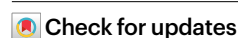


Threat of low-frequency high-intensity floods to global cropland and crop yields

Received: 2 August 2023

Accepted: 15 May 2024

Published online: 24 June 2024



Jichong Han^{1,2}, Zhao Zhang¹✉, Jialu Xu¹, Yi Chen³, Jonas Jägermeyr^{4,5,6}, Juan Cao¹, Yuchuan Luo⁷, Fei Cheng¹, Huimin Zhuang¹, Huaqing Wu¹, Qinghang Mei¹, Jie Song^{1,2} & Fulu Tao^{1,2}✉

Flood hazards pose a significant threat to agricultural production. Agricultural adaptations tend to be prevalent and systematic in high-frequency flood (HFF) areas but neglected in low-frequency flood (LFF) areas. Here, using satellite imagery, we map global spatial distributions of LFF and HFF at 250 m resolution for 3,427 flood events between 2000 and 2021. We show that LFF affected a larger proportion of cropland area (4.7%) than HFF (1.2%), and HFF occurred in smaller regions with less intensity. Cropland expansion between 2000 and 2019 increased the area affected by LFF ($3.1 \times 10^4 \text{ km}^2$) more than that affected by HFF ($1.3 \times 10^4 \text{ km}^2$). Moreover, the mean yield losses of wheat and rice from LFF were greater than those from HFF, owing to the higher precipitation anomalies, soil moisture anomalies and greater crop flooding during their growing seasons. Our findings highlight the urgency of this issue and identify priority areas to prevent these neglected low-frequency but high-impact floods, providing valuable information for developing flood-adapted policy.

Floods affect agricultural production widely across the world^{1,2}. Although numerous studies have reported the impacts of drought and heat stress on global crop yields, the impacts of floods have been less studied because most current crop models are not well developed in representing the impact processes of flooding and excess moisture^{3–7}. Flooding poses a significant threat to global agricultural production, and this threat may increase as floods are projected to become more frequent and severe in many breadbasket regions under future climate change^{8–10}. A comprehensive impact assessment of future floods on global agricultural production is therefore critical to identifying adaptation priorities.

Recently, some studies applied process-based crop models or satellite-based damage indices to investigate yield losses from floods regionally^{11–13}. Process-based crop models are generally used

to attribute the spatiotemporal change in flood-induced crop yield losses¹⁴. These models are improved to simulate the impacts of flooding or waterlogging on crop phenology, photosynthesis, nitrogen uptake, grain formation and yield penalties, but they are still at an infant stage^{6,12,14}. Some studies use extreme precipitation as an indicator, but without accounting for land surface characteristics, which can lead to misrepresented impacts as flooded areas often occur downstream from the precipitation areas^{14–16}. A study based on crop yield statistics showed that drought and heat stresses lead to severe yield losses at the national level, whereas the impacts of floods are insignificant because they generally occur more regionally⁴. Flooding areas can be precisely captured by medium- to high-resolution inundation maps from satellite observations. However, climate and yield data with a coarser spatial resolution make it difficult to quantify the exposure of crop production

¹Joint International Research Laboratory of Catastrophe Simulation and Systemic Risk Governance, School of National Safety and Emergency Management, Beijing Normal University, Beijing, P. R. China. ²School of Systems Science, Beijing Normal University, Beijing, P. R. China. ³Key Laboratory of Land Surface Pattern and Simulation, Institute of Geographical Sciences and Natural Resources Research, Chinese Academy of Sciences, Beijing, P. R. China. ⁴NASA Goddard Institute for Space Studies, New York, NY, USA. ⁵Center for Climate Systems Research, Columbia University, New York, NY, USA. ⁶Potsdam Institute for Climate Impacts Research, Leibniz Association, Potsdam, Germany. ⁷Chongqing Jinpo Mountain Karst Ecosystem National Observation and Research Station, School of Geographical Sciences, Southwest University, Chongqing, P. R. China. ⁸College of Resources and Environment, University of Chinese Academy of Sciences, Beijing, P. R. China. ✉e-mail: zhangzhao@bnu.edu.cn; taofl@igsnr.ac.cn

to floods, especially at a national or global scale^{15,17}. Previous empirical studies are thus often limited by the lack of crop yield statistics at a subnational scale⁴, which render it difficult to accurately assess crop yield changes associated with flooding globally. A spatially explicit global archive of historical flooding events will help strengthen the flood–yield relationship and develop adaptation strategies, but it has been available rarely so far.

Flooding frequency varies by region^{2,18,19}. We categorized these events into low-frequency floods (LFF) and high-frequency floods (HFF) according to annual flooding frequency. We defined an area as an LFF (HFF) area if the frequency of flood-event occurrence was <0.5 (≥ 0.5) within a six-year window (Supplementary Figs. 1, 7 and 8). Compared with HFF, LFF are usually linked to extreme precipitation events with a lower inundation frequency, larger precipitation anomalies and higher flood intensity. Global cropland areas have continuously been expanded²⁰, but the dynamics of cropland exposed to flooding have rarely been quantified. It is generally believed that floods cause severe crop losses in HFF areas but less in LFF areas¹³. However, several regional studies have documented higher crop yields in flood-prone areas^{21,22}, and floods were more destructive in arid areas than in wet areas²³. Differing outcomes of LFF and HFF for crop yields, including effects on nutrient deposition and soil-moisture replenishing, need to be further investigated at a global scale to develop adaptations to changing floods.

To address these limitations, we have tried to improve the flooding impact assessment by combining new flooding maps retrieved from satellite observations and global hazard datasets using a near-real-time algorithm²⁴. We used satellite images to develop a global database of LFF and HFF areas at 250 m spatial resolution for 3,427 flood events between 2000 and 2021. We overlaid the inundation area layers with the cropland layer to identify the flood-affected cropland for each flood event. We then explored the global spatial distribution of LFF- and HFF-affected croplands for all the flood events. Next, we analysed annual dynamics of cropland exposed to floods, and finally we quantified crop yield losses from the flood events on the basis of the subnational yield data collected from official websites (Methods). We analysed the mean differences in wheat and rice yield losses in LFF and HFF areas at the global scale. Using our developed global long-term high-resolution flood maps, along with the subnational-level yield data, we can better quantify the impact of flooding on global crop yields through empirical analysis. The different drivers controlling yield losses from LFF and HFF are investigated comprehensively by integrating crop phenology, precipitation, soil moisture anomalies and crop growth anomalies together.

Results

Frequency, duration and area of cropland exposed to floods

We generated flood maps with 250 m resolution for 3,427 flood events recorded in the Dartmouth Flood Observatory (DFO) catalogue (Supplementary Fig. 2). The accuracy of the flood maps was evaluated using 33,141 publicly available sample points from third parties²⁵ based on Landsat image interpretation of 123 flood events with a resolution of 30 m (Supplementary Fig. 3). The accuracy decreases with increasing duration of the flooding event in regions at latitudes $<45^\circ$; by contrast, it increases and then decreases with increasing duration in regions at latitudes $\geq 45^\circ$ (Supplementary Fig. 4). This indicates that the approach overestimates flooding extent at high latitudes mainly because of low-reflectance objects similar to water bodies, caused by low solar angles²⁶. We therefore kept the related flooding areas with a duration ≥ 4 days for the 306 flooding events (latitude $\geq 45^\circ$) because of their higher accuracy (Supplementary Fig. 5). The overall accuracy of flood detection is 0.78, with a commission error of 0.26 and an omission error of 0.21 (Supplementary Fig. 6). The details of two typical flood events are presented in Supplementary Figs. 9 and 10. Compared with a previous study²⁵, we improved flood detection as follows: (1) mapping of additional flood events, (2) distinguishing LFF from HFF, (3) redefining

the flood duration dates (the earliest to the latest dates of water bodies observed by satellite during the event) and (4) correcting the accuracy of flood maps at high latitudes.

We calculated the frequency of cropland exposed to flooding by aggregating the counts of flooding-affected areas within a $1^\circ \times 1^\circ$ grid (Methods). The HFF areas were mainly distributed in Southeast Asia, southern China and the south-central United States (Fig. 1a–c). By contrast, the LFF areas were scattered globally. The mean duration was 3.5 days for LFF and 10 days for HFF, without significant duration differences across flooding areas (Fig. 1d–f). About 1.02×10^6 km² of global cropland had experienced at least one flooding event since 2000. LFF and HFF affected 4.7% and 1.2% of global croplands, respectively (Fig. 1g–i). The countries with the largest areas of flooding-prone croplands were India, China, the United States and Russia (Fig. 1j and Supplementary Fig. 11). However, other countries (for example, Thailand, Vietnam, Cambodia and Madagascar) had smaller absolute cropland areas exposed to flooding but a higher percentage of exposure areas. Flooding may severely threaten crop production in these countries.

We further analysed the sensitivity of the largest cropland area affected by floods globally to the missing data of flood events (Supplementary Fig. 12). The frequency, duration and area of cropland exposed to LFF and HFF with different thresholds show a strong linear relationship (Supplementary Fig. 13). As the threshold increases, the frequency and area of cropland exposed to LFF increase, while those exposed to HFF decrease.

Increased flooding risk from cropland expansion

Potapov et al.²⁰ showed that global cropland areas exhibited a significant upward trend from 2000 to 2019 (Supplementary Fig. 14; $P < 0.05$). Conversely, we found that the cropland areas exposed to LFF and HFF showed a decreasing trend ($P < 0.05$), which is consistent with those recorded by DFO (Supplementary Figs. 14 and 15). Human activities have driven the expansion of cropland^{27,28}. Changes in flood-affected cropland directly reflect the impacts of human activities on cropland exposure to flooding inundation (Fig. 2 and Supplementary Figs. 16 and 17).

Cropland expansion resulted in an increase in LFF-affected cropland in southern Asia, central South America, central and southern Africa, and eastern North America (Fig. 2a,b). By contrast, cropland conversion led to a decrease in HFF-affected areas in southern Europe, eastern North America and southern China (Fig. 2a,b). Additionally, the increase in HFF-affected cropland caused by cropland expansion was primarily concentrated in South Asia (Fig. 2c,d).

The increased cropland areas exposed to LFF and HFF from 2000 to 2019 reached 3.1×10^4 km² and 1.3×10^4 km², respectively. Moreover, the net area changes exposed to both LFF and HFF due to cropland change increased (Fig. 2f–h). Our findings highlight that global flooding risk increased due to cropland expansion despite a decreasing trend in total flooding areas. The sensitivity analysis shows that the trend in cropland area affected by floods is consistent using different thresholds in classifying LFF and HFF (Supplementary Fig. 18). The changes in cropland area exposed to floods, classified using different thresholds, have a strong linear relationship spatially (Supplementary Fig. 19). As the thresholds increase, the cropland area exposed to LFF increases, while it decreases for HFF. The net change trend in global cropland area exposed to floods is consistent using different thresholds (Supplementary Fig. 20).

The top three countries with the highest net increase (decrease) in LFF areas from cropland change were India, the United States and China (Mexico, Tanzania and Uruguay) (Fig. 2e–g). For HFF-affected cropland, the top three countries with the highest net increase (decrease) due to cropland change were India, Bangladesh and China (Ghana, Iraq and the United Kingdom). Bangladesh and China showed a relatively smaller net change for HFF, but with a higher increase and decrease. The net change in Brazil was relatively small, but the changes in HFF areas were relatively higher.

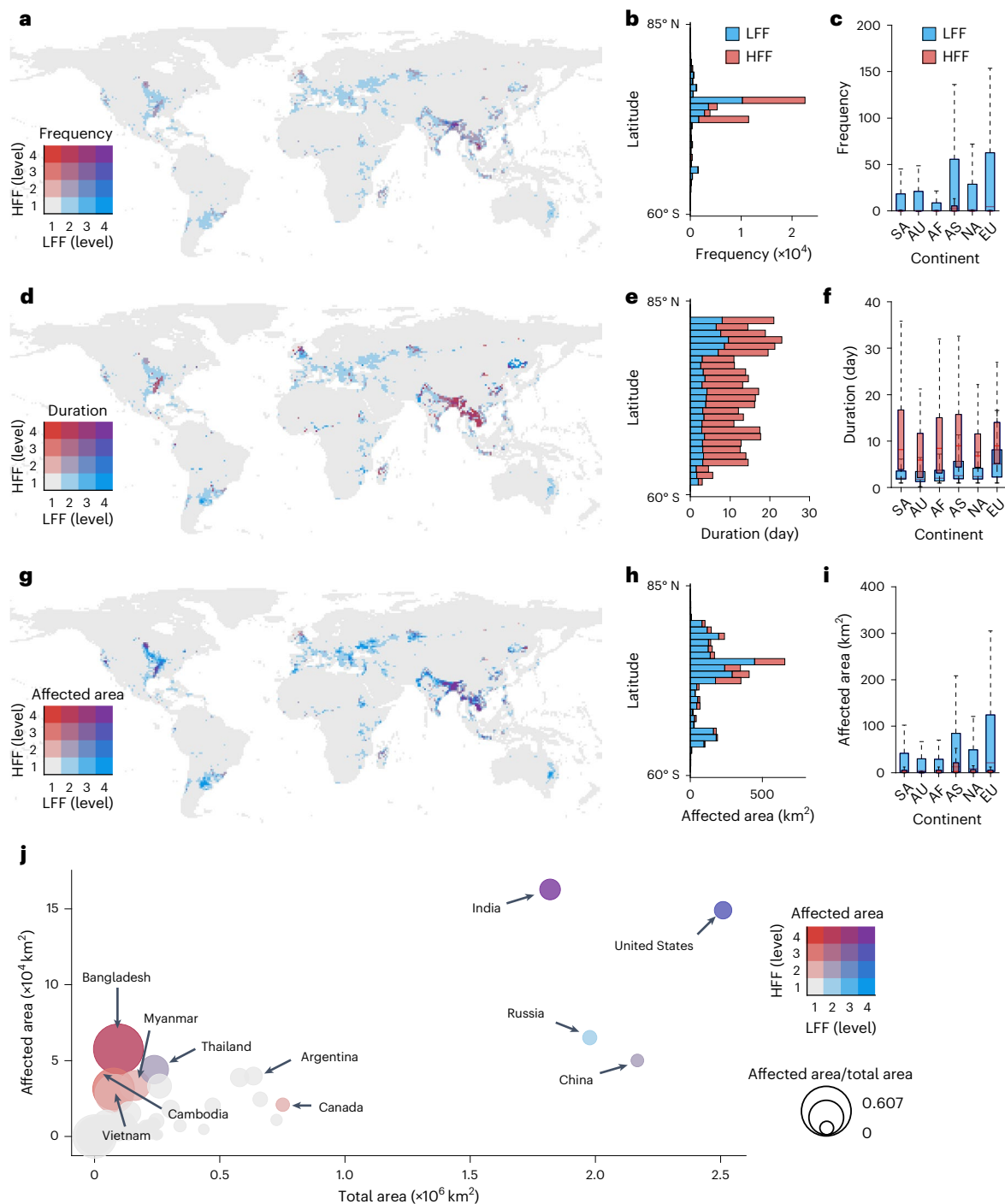


Fig. 1 | Global patterns of cropland exposed to flooding from 2000 to 2021. **a,d,g**, Spatial distribution of frequency (**a**), mean duration (**d**) and maximum flooding area of cropland (**g**) in the $1^\circ \times 1^\circ$ grid. **b,e,h**, Latitudinal profiles of mean frequency (**b**), mean duration (**e**) and maximum flooding area (**h**) of cropland in different latitudinal zones. **c,f,i**, Flooding characteristics at the continental scale. In each box plot, the central line indicates the median, the lower and upper boundaries of the rectangle indicate the first and third quartiles, and the whiskers extend to the maximum value of 1.5 times the interquartile range. SA, South and Central America; AU, Australia; AF, Africa; AS, Asia; NA, North America; EU, Europe. Grid counts: $n = 6,638$ (LFF), $n = 4,671$ (HFF). **j**, Flood-affected cropland at the national level. The scatter plot shows the absolute affected area per country; the circle size indicates the fraction of a nation's cropland affected (the ratio of the maximum flooding area to the total cropland area). The thresholds for the frequency levels are $50, 5 \times 10^4$ and 15×10^4 ; for the duration bins, 1, 10 and 20 days; and for the affected area bins, $1, 5 \times 10^2$ and 1×10^3 km². The flood map has a spatial resolution of 250 m and is aggregated into a 1° grid for clear visualization.

We further analysed the specific land cover and land use types that were replaced by cropland in global cropland exposure (Fig. 2i,j and Supplementary Figs. 21 and 22). Over the past 20 years, the net change in cropland exposed to LFF and HFF due to cropland change increased.

In LFF areas, 54% of cropland expansion areas were converted from wetlands and short vegetation, with countries such as the United States, China and India having higher proportions (Supplementary Figs. 21 and 22), and 3% were converted from trees. In HFF areas, the conversion

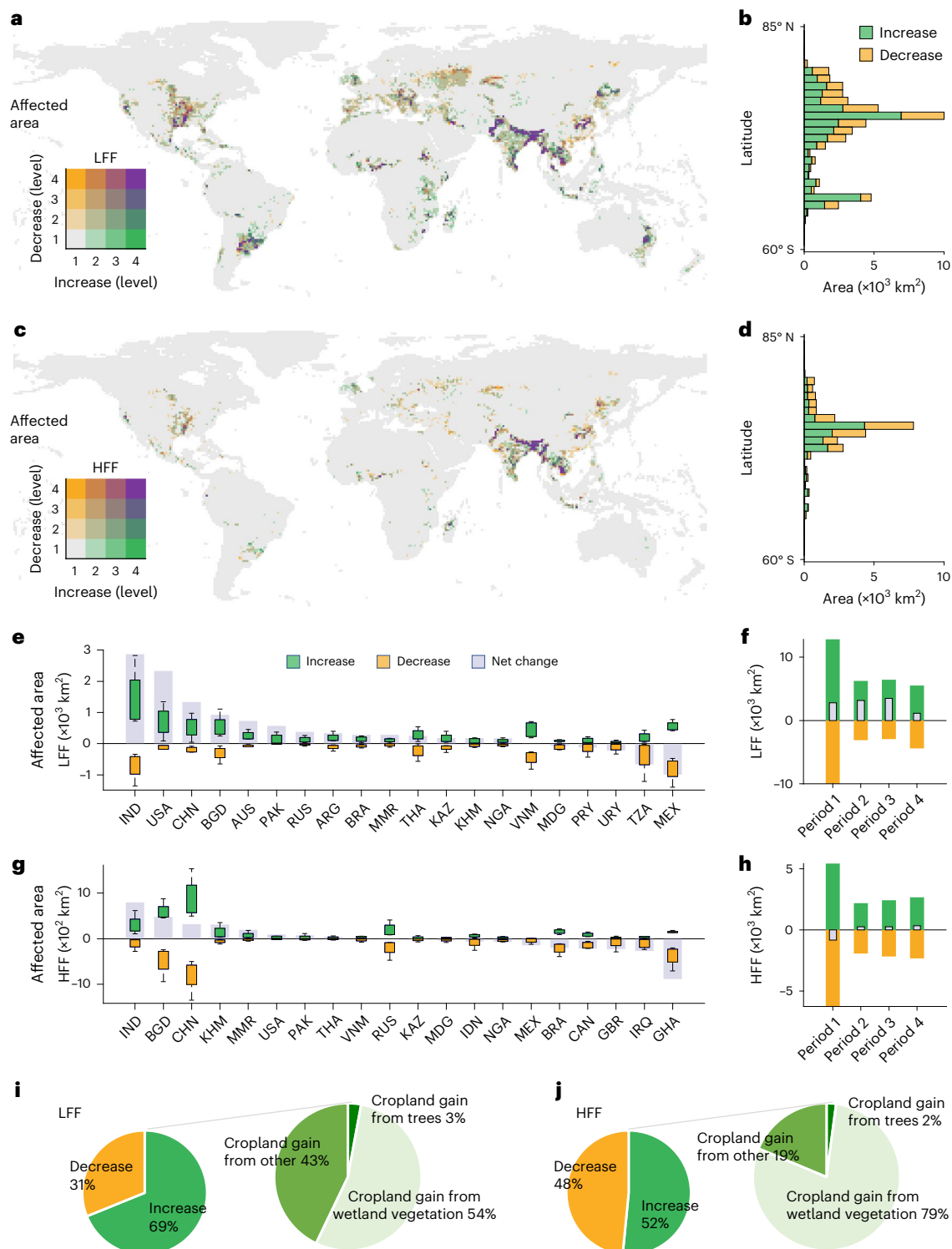


Fig. 2 | Changes in flood-affected cropland area due to global cropland change from 2000 to 2019. a,c, Flooding area change on a $1^\circ \times 1^\circ$ grid for LFF (a) and HFF (c). **b,d,** Flooding area change in different latitudinal zones. **e,g,** National cropland changes during different periods (only the top ten countries with relatively larger net area change are listed), with ISO-alpha3 country codes. In each box plot, the central line indicates the median, the lower and upper boundaries of the rectangle indicate the first and third quartiles, and

the whiskers extend to 1.5 times the interquartile range. $n = 4$ (periods 1–4). The periods 1–4 are defined as every four years continually (2000–2003, 2004–2007, 2008–2011, 2012–2015 and 2016–2019). **f,h,** Global area changes over different periods with all changes calculated as the differences between two adjacent periods (the latter years minus the previous ones). The thresholds for LFF/HFF levels are 1, 10 and 20 km². **i,j,** The specific land cover and land use types converted to cropland in the past 20 years.

from wetlands and short vegetation accounted for 79%, with the highest proportions in countries such as India and Bangladesh (Supplementary Figs. 21 and 22).

Greater crop yield losses from LFF than from HFF

On the basis of the Global Flood Database and the improved subnational crop yield statistics (Supplementary Fig. 23), we estimated the

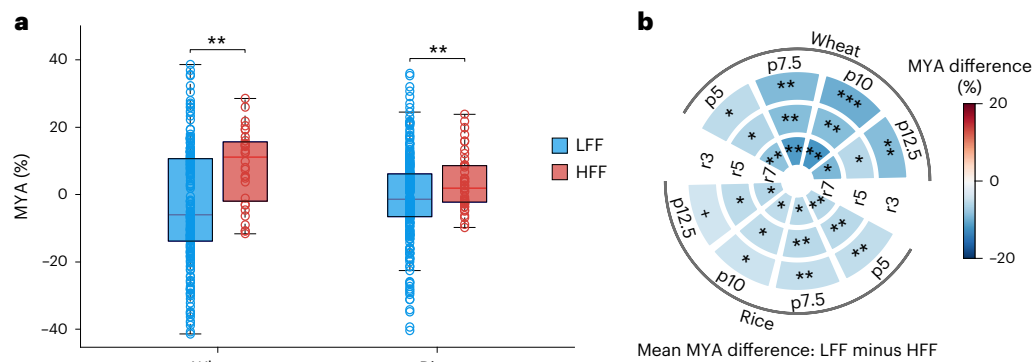


Fig. 3 | MYA in LFF and HFF areas. a, MYA are calculated using a five-year moving mean based on samples with flooding area >7.5% of the total cropland area, with the same box plot components as those in Fig. 1 (significant samples at the 10% significance level using 10,000 iterations of the bootstrap). In each box plot, the central line indicates the median, the lower and upper limits of the rectangle indicate the first and third quartiles, and the whiskers extend to the maximum value of 1.5 times the interquartile range. Significance was determined using a Wilcoxon test (*** $P < 0.001$; ** $P < 0.01$; * $P < 0.05$; $P < 0.1$). The statistical tests were

two-sided, and no adjustments were made for multiple comparisons. The sample sizes (n) and P values can be found in Supplementary Table 1. **b**, The different MYA from LFF and HFF were calculated on the basis of samples with different moving thresholds (r3–r7 for the moving means of 3, 5 and 7 years) and sampling rules (p5–p12.5 for inundated area percentages of total cropland area from 5% to 12.5% with a 2.5% interval). The sample sizes (n) and P values can be found in Supplementary Table 1. Blue represents higher yield losses in the LFF areas than in the HFF areas, while red is the opposite.

mean yield anomalies (MYA) of wheat and rice from LFF and HFF during the studied period at the subnational scale (Supplementary Fig. 24). Wheat and rice yields decreased on average by 4.0% and 1.2% from LFF but increased by 4.6% and 4.2% from HFF (Fig. 3a), indicating greater mean yield losses from LFF than from HFF ($P < 0.05$). These findings are supported by a previous study reporting higher rice yields in flooding-prone areas²¹. Further analyses show that the results are not strongly influenced by the sample size (Supplementary Fig. 25). These findings substantiate the idea that the high-resolution flooding maps and the better match between areas exposed to floods and detailed yield records improve the estimates of yield losses at the global scale. Previous studies neglected important information such as geography, floods and mismatch between areas exposed to flooding and actual crop yields, making it difficult to accurately quantify crop yield losses from floods⁴. To test the robustness of yield loss differences from LFF and HFF, we compared the different moving means and screening rules (Methods) and found that the differences are consistent (Fig. 3b and Supplementary Fig. 26). Moreover, we confirmed that the yield losses from LFF were consistently greater than those from HFF with different thresholds for defining LFF and HFF (Methods) (Supplementary Figs. 27 and 28). We further quantified the uncertainty in estimating the MYA using Monte Carlo simulations (Supplementary Fig. 29), which enhances the reliability of our results.

Drivers of yield losses in LFF and HFF

The relationship between global floods and crop phenology has rarely been investigated. DFO records from 2000 to 2021 show latitudinal heterogeneity in the months when global floods begin and end (Supplementary Fig. 30). Floods occur mainly in June–August at mid-latitudes and in January–February at low latitudes; these differences are associated with the seasonality of precipitation along latitudinal zones²⁹. The significance of the associations between flood timing and vegetation phenology has been highlighted³⁰. Since crop phenology is not available in the DFO data, we used phenological data derived from satellite images to identify crop growth stages during inundation periods at the pixel scale (Fig. 4 and Supplementary Figs. 31–33).

Floods occurring during the growing season (GS) caused larger yield losses than those in the non-growing season (NGS). LFF occurred more frequently during the GS than HFF did in all latitudinal zones (Fig. 4a,b,d,e,g,h,j,k). Longer growing periods in LFF areas at higher latitudes tend to increase the exposure possibility to floods during the GS³⁰. In contrast, a larger proportion of crops in HFF areas (for

example, Southeast Asia) is in the NGS when floods occur. The farmers in Southeast Asia rely on floodplain farming, including flood-irrigated and flood-fallow cropping systems²¹, where planting timing is mainly dependent on flooding time rather than any other preferences^{2,31}. The farmers in such HFF areas are therefore usually used to taking advantage and avoiding the disadvantages of floods, adapting their farming practices to the local environment.

We further analysed the proportion of inundated areas during the GS on the basis of crop samples significantly affected by floods (Fig. 4c,i). The results indicate that crops had significantly higher proportions of inundated areas during the GS by LFF than those by HFF ($P < 0.05$). Additionally, as the proportion of flooded crop area during the GS increases, the mean yield loss also increases (Supplementary Fig. 34), indicating the impact of the timing of floods on crop yield. The consistently significant differences between LFF and HFF were confirmed by comparing different moving-mean methods and screening rules (Fig. 4f,i). Additionally, by replacing remotely sensed phenology with crop calendars calculated from the Global Gridded Crop Model Intercomparison product³², we found the same differences between LFF and HFF (Supplementary Fig. 35). Furthermore, even with different thresholds in defining LFF and HFF, a greater proportion of crops during the GS were affected by LFF than by HFF (Supplementary Figs. 36 and 37).

We found that precipitation and soil moisture anomalies (PA/SMA) were more significant from LFF than from HFF ($P < 0.05$), especially for SMA (Fig. 5a,b,d,e). Floods were mainly associated with soil saturation status^{33,34} and significantly correlated with soil moisture³⁵. Using most data products and different methods, we confirmed that the global average precipitation and soil moisture during flood events in LFF areas are significantly higher than those in HFF areas (Fig. 5g,h,j,k), although there is a possibility of severe flood events due to extreme climate in HFF areas.

Vegetation indexes have been widely applied to monitor crop growth and assess the impacts of climatic events. We generated global two-band enhanced vegetation index (EVI2) time series data (2000–2021) to test their different responses to LFF and HFF. Our analyses reveal a higher proportion of both short- and long-term EVI2 anomalies from LFF than from HFF after floods (Supplementary Figs. 38–42). When the long-term impacts were compared with the short-term impacts, the EVI2 anomalies from both LFF and HFF decreased because of low flooding damage and consequent recovery from the floods³⁶. However, long-term EVI2 anomalies did exist, suggesting that the

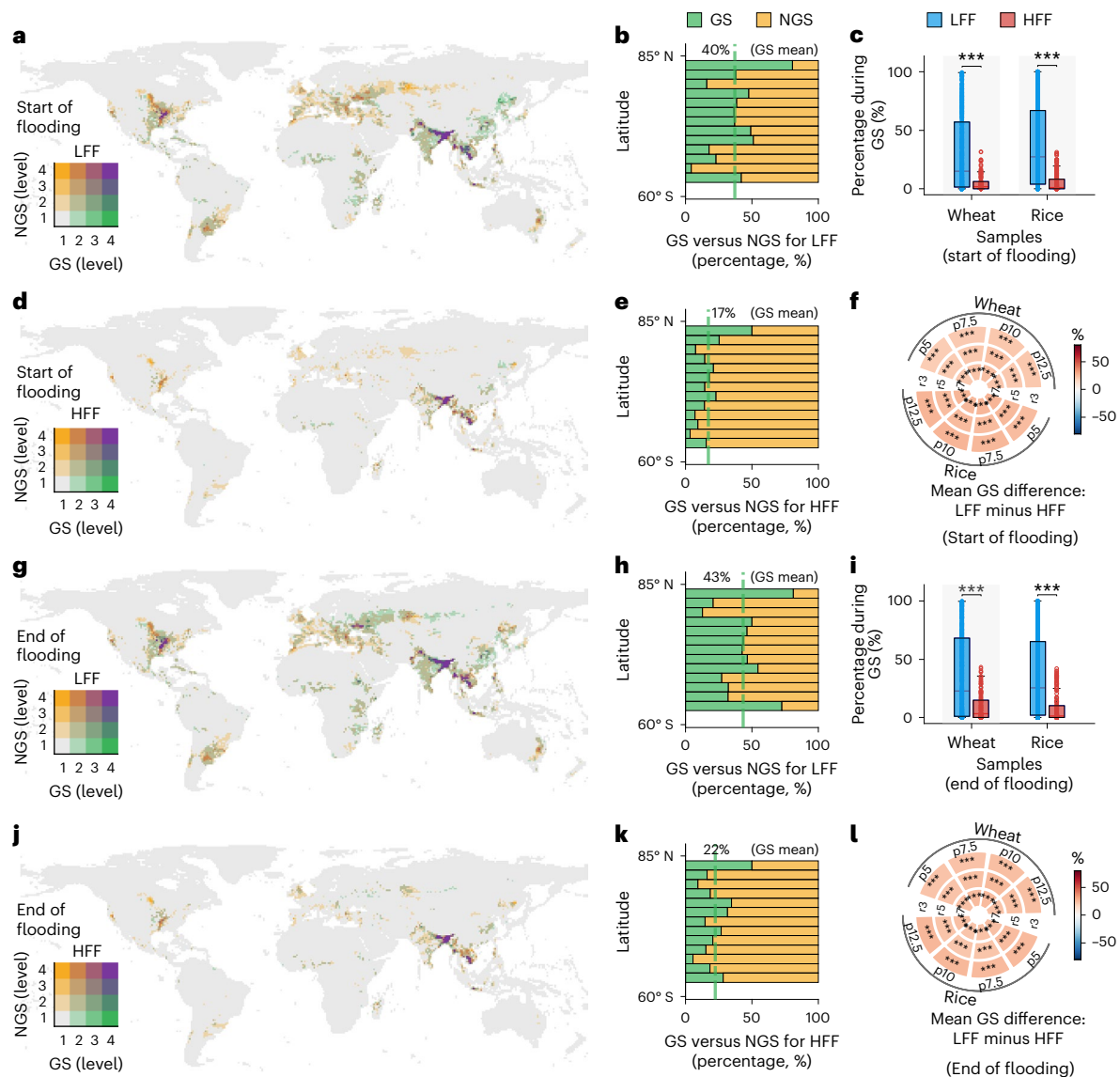


Fig. 4 | Relationship between the inundation period and crop phenology during flooding events (2000–2021). **a,d,g,j.** Spatial distribution of crop GS and NGS falling within the inundation periods of LFF (**a,g**) and HFF (**d,j**) events in $1^\circ \times 1^\circ$ grid cells at the beginning (**a,d**) and end of flood events (**g,j**). **b,e,h,k.** The proportion of GS and NGS areas in different latitudinal zones. **c,i.** The proportion of inundated cropland areas during the GS to total flooding cropland areas based on samples of wheat and rice in LFF and HFF zones at the beginning (**c**) and end of flood events (**i**), with the same samples as those in Fig. 3a. In each box plot, the central line indicates the median, the lower and upper limits of the rectangle indicate the first and third quartiles, and the whiskers extend to the

maximum value of 1.5 times the interquartile range. Significance was determined using a Wilcoxon test ($***P < 0.001$). The statistical tests were two-sided, and no adjustments were made for multiple comparisons. **f,l.** The difference in the proportion of the GS in LFF and HFF areas at the beginning (**f**) and end of flood events (**l**), with positive values (red) meaning that a greater proportion of the GS fell within the inundation periods of LFF than those of HFF, with the same samples as those in Fig. 3b. The sample sizes (n) and P values can be found in Supplementary Tables 1 and 4. The thresholds for LFF/HFF levels are 10, 500 and 1,000 km^2 .

damage to crop growth may be severe³⁶. For instance, the rice EVI2 curve in the Huai River basin of China increased continuously until the tasselling stage and then dropped abruptly after the flood in July 2003 and recovered eventually (Supplementary Fig. 41).

We further analysed the EVI2 anomalies on the basis of crop samples significantly impacted by floods (Fig. 5c,f). We found that crop growth anomalies were higher in LFF than in HFF, with more significant differences for rice than for wheat for short-term impacts. When the differences between short-term and long-term impacts were compared, the EVI2 anomalies decreased more in LFF than in HFF (Fig. 5c,f). Compared with HFF, the shorter duration of LFF (Fig. 1d–f) may imply a higher crop resilience³⁶. Further analyses indicate that our sample size is sufficient (Supplementary Figs. 43 and 44), and the results are similar

to different moving means, different screening rules (Fig. 5g–i) and different LFF and HFF threshold definitions (Supplementary Figs. 45 and 46). The factor uncertainty analysis using Monte Carlo simulations (Supplementary Fig. 47) further substantiates the reliability of our findings. Excessive moisture is more commonly observed in HFF areas, which may pose specific challenges for crop growth. In LFF areas, crops are more likely to be destroyed, thus necessitating more adaptations.

Discussion

The impacts of floods on crop yield are determined by factors such as crop phenology and flood intensity³⁷, which can be reflected by crop growth status³⁸. PA and SMA can indirectly reflect flood intensity³⁹. Our results reveal a significant positive correlation ($P < 0.05$;

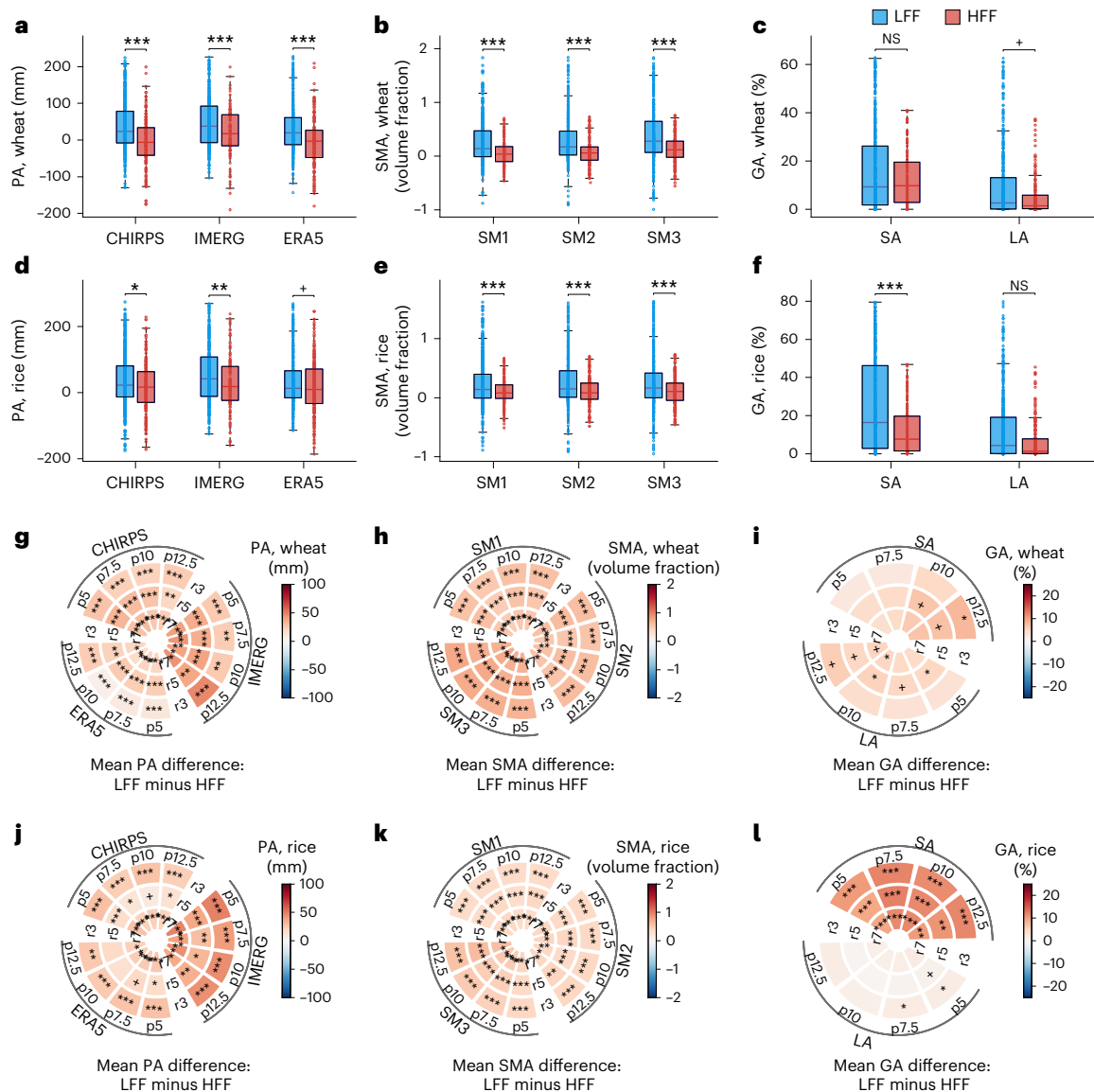


Fig. 5 | PA/SMA during flooding and crop growth anomalies after flooding.

a–f, Precipitation products: Climate Hazards Group InfraRed Precipitation with Station data (CHIRPS), Integrated Multi-satellite Retrievals for Global Precipitation Measurement (IMERG) and ECMWF Reanalysis v.5 (ERA5). SM1–SM3 indicate different soil layers (0–7 cm, 7–28 cm and 28–100 cm). GA is the percentage of the total area of flooded cropland with negative crop growth anomalies after flooding. SA, short-term growth anomaly; LA, long-term growth anomaly. In each box plot, the central line indicates the median, the lower and upper limits of the rectangle indicate the first and third quartiles, and the whiskers extend to maximum value of 1.5 times the interquartile range. Significance was determined using a Wilcoxon test (*** $P < 0.001$; ** $P < 0.01$;

* $P < 0.05$; * $P < 0.1$; NS, not significant). The statistical tests were two-sided, and no adjustments were made for multiple comparisons. **g–l**, Differences in PA, SMA at different depths and negative growth anomalies in areas with LFF and HFF for samples with significant yield anomalies calculated on the basis of the moving mean method with different thresholds (r3–r7 for the moving means of 3, 5 and 7 years) and different screening rules (p5–p12.5 for inundated area percentages of total cropland area from 5% to 12.5% with a 2.5% interval). The samples used in this analysis are the same as those in Fig. 3a (a–f) and Fig. 3b (g–l). The sample sizes (n) and P values can be found in Supplementary Table 1 and Supplementary Tables 5–7.

Supplementary Fig. 48) between GS, PA, SMA and negative growth anomalies during flood events, and a significant negative correlation ($P < 0.05$; Supplementary Fig. 49) between GS, PA, SMA and MYA. The significant differences in GS and PA/SMA between LFF and HFF areas should be potential contributors to the differences in crop yield losses between them. In seasonally inundated regions, people may experience more frequent flooding events but may not necessarily be more vulnerable²; instead, they may use natural flood cycles to develop fisheries and agriculture. Populations engaged in flood recession agriculture benefit from seasonal floods and rely on their predictability². For example, rice fields depend on specific quantities of flooding, which explains why the proportion of the GS is lower during flood events in HFF areas.

There is evidence indicating that in regions with frequent flooding, people tend to adopt more agricultural adaptation measures. For instance, in Bangladesh, farmers have already started adopting adaptive agricultural techniques such as floating farms⁴⁰. In North Agusan, the Philippines, farmers have adapted by altering their cultivation practices⁴¹. In contrast, in areas with infrequent floods, residents are less prepared and adapted to sudden flood events, and the construction of dams and levees is not a priority project²³.

We also conducted cropland exposure, yield loss estimation and sensitivity analysis in local watershed areas in Bangladesh, concentrating on LFF and HFF areas, using the same methods as at the global scale (Supplementary Figs. 50–52). The sensitivity analysis in these local

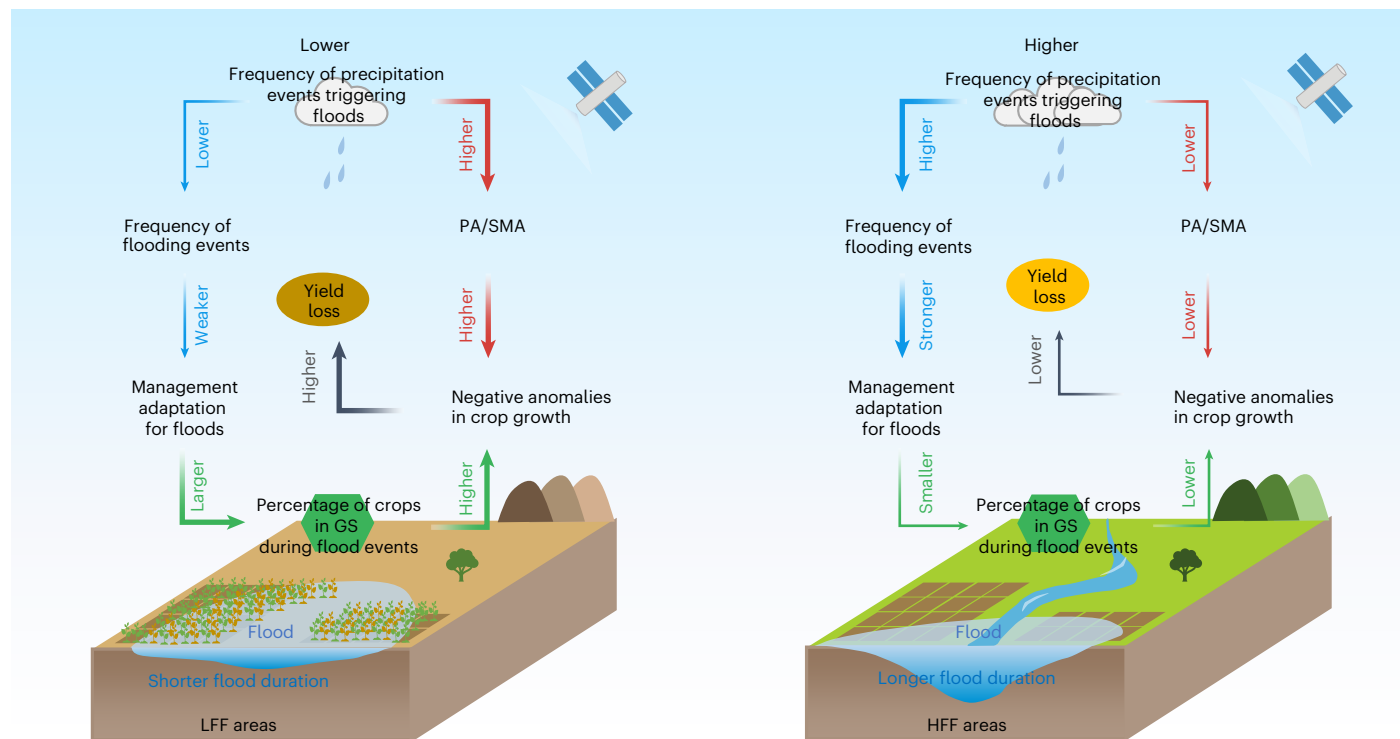


Fig. 6 | Different crop yield impacts from LFF and HFF. The mechanisms underlying the disparities in crop yield impacts from LFF and HFF. The blue arrows indicate connections among the frequency of precipitation events triggering floods, the frequency of flooding events and management adaptation for floods. The red arrows indicate connections among the frequency of

precipitation events triggering floods, PA/SMA and negative anomalies in crop growth. The green arrows indicate connections among management adaptation for floods, the percentage of crops in GS during flood events and negative anomalies in crop growth. The gray arrows indicate the final impact on yield loss. Arrow width corresponds to effect magnitude.

areas is similar to that at the global scale. We used a unified threshold to classify LFF and HFF globally for comparisons across different regions worldwide in this study. Owing to specific agricultural climate conditions in each region⁴² (Supplementary Fig. 53), flood frequency might be relative. We further analysed the impact of floods on crop yield when using different thresholds to define LFF and HFF in agricultural zones (Methods). We found that even with different thresholds, the mean global crop yield losses remain higher in LFF areas than in HFF areas (Supplementary Figs. 54 and 55), and the results are similar in different sensitivity tests. Consistent conclusions were also drawn from the influencing factors analyses (Supplementary Figs. 56 and 57).

In sum, the flooding processes from initial precipitation to final yield losses are complex and controlled by multi-factor interactions, which are illustrated separately for LFF and HFF in Fig. 6. In LFF areas, the frequency of precipitation events that trigger flooding is lower, and farmers often have less flood risk prevention and rarely adapt measures such as capacity building for preventing floods, planting flood-tolerant crop varieties or adjusting sowing dates to reduce flood damage⁴³. In LFF systems, a larger proportion of crops is grown with high exposure to flooding. Furthermore, high PA/SMA in these LFF areas cause larger damage to crops in their GS, resulting in larger yield losses. In contrast, in HFF areas, heavy precipitation events trigger floods more frequently, and farmers have often implemented various measures to cope, including drainage systems, changing planting dates to avoid flooding periods or using flood-tolerant varieties^{2,21,31}. Moreover, frequent floods generally bring mineral-rich silt to cropland, and, together with smaller PA/SMA, on average cause smaller crop yield losses in HFF areas. Our study provides insights into the mechanisms underlying the different impacts from LFF and HFF.

The reasons for cropland expansion in HFF and LFF areas are diverse. In HFF areas, despite the higher flood risk, floods bring

sediment, which increases soil fertility⁴⁴. HFF areas are usually closer to water sources, which is advantageous for irrigation and agricultural production². With technological progress such as the construction of levees and dams, some areas that previously experienced frequent flooding may become more suitable for agricultural production; the expansion of cropland in flood-prone areas is therefore increasing². In LFF areas, the land may be perceived as safer and more suitable for long-term agricultural development due to fewer floods. Additionally, increasing population growth and food demand as well as land policies may promote the expansion of cropland in flood-prone areas²⁰.

The impacts of floods on agricultural production are complex and context-dependent^{37,45}. Frequent but less intense floods may create suitable habitats for rice, yet might be harmful for wheat. For example, in the southeastern United States, rainfall significantly reduced wheat yields but had little impact on corn and rice yields⁴⁶. Floods may occur before the planting season, preventing farmers from planting or shortening the GS. However, it is challenging to identify the areas where floods prevent farmers from planting in all flood events at the global scale. In the global flood events recorded by the DFO, there is no recorded information on farming activities, which limits our further analysis. In addition, the effects of floods on crop yield differ by timing¹⁴. Although our analysis resolution is significantly better than that of previous national-level study⁴, the complexity of crop growth and phenological variability within subnational units makes it difficult to finely quantify the impacts on yield at different phenological stages at the global scale. The detailed field trial data at the site scale should be exploited to investigate the impact processes of floods on crop growth and yield at different phenological stages¹⁴.

We compiled an initial global database of LFF and HFF, including 3,427 flooding events from 2000 to 2021; integrated detailed crop phenology into the new database; and identified factors driving different

yield losses between LFF and HFF. We found that the mean duration of HFF was longer than that of LFF for all flood events globally, while the area affected and the global mean yield losses from LFF were higher than those from HFF. Cropland expansion has amplified the flooding risk from LFF, especially during recent years. Compared with previous studies focusing on exposure, risk or vulnerability of crops to floods, this study broadens the perspective, discovers the mechanisms, underscores the urgent need and identifies priorities to prevent losses from low-frequency but high-impact flood hazards. Some limitations exist in the study. One is the uncertainty from the standard thresholds for identifying water bodies in the flood extraction algorithm, which may cause a bias of flooding extent in some cases²⁵. High cloud presence can lead to an underestimation of actual flooding areas, causing uncertainties in estimating yield effects, especially in tropical regions (Supplementary Fig. S8). Nevertheless, the main conclusions from this study are robust, given the consistent results using different methods, thresholds and definitions. Another limitation is that flood events are categorized into only two coarse types (LFF and HFF). Finally, a more accurate crop area layer would improve yield loss estimates. The framework proposed here is applicable to assessing global flooding impacts on other crops as well. Our findings highlight that adaptation measures should be developed to target low-frequency but high-impact flood hazards, providing timely and valuable information for strengthening and developing flood-adapted management measures to cope with increasing flood risk under future climate change. The combination of empirical inferences, process-based models and satellite observations should be applied to deepen the understanding of extreme climate impacts on agriculture¹⁴.

Methods

Global active archive of large flood events

We collected 5,130 global flood events from the DFO from 1 January 1985 to 6 October 2021 (Supplementary Fig. 2). Flood information recorded by the DFO is derived from news, governments, instruments and remote sensing imagery. This database is widely regarded as one of the most comprehensive resources for documenting historical flood events⁴⁷. Many previous studies have focused on either rainfall-based datasets or model-based stream flow data⁴⁸. The DFO flood database also provides information about trends in major flood events over time^{25,47}.

Flood extent and duration extraction algorithm

We used MODIS imagery from NASA's Terra (MOD09GA/GQ061) and Aqua (MYD09GA/GQ061) satellites to identify floods. We excluded AVHRR imagery from datasets from earlier years (5,566 m resolution) due to MODIS's higher spatial resolution (up to 250 m). We also did not use Landsat satellites with a spatial resolution of 30 m because their 16-day revisit cycle missed a large number of the actual flooded areas. Our analysis identified 3,427 flood events that overlapped with the MODIS image data from 2000–2021 (Supplementary Fig. 2). For each flood event, we selected all HydroSHEDS Basins Level 6 watersheds⁴⁹ that intersected with the flood event polygons as the mapping extent. We screened all daily MODIS images within the geographic extent and date range of each flood event. An existing near-real-time flood extraction algorithm based on reflectance and standard thresholds (equation (1)) was applied to classify water body pixels on all MODIS images^{25,50}.

The daily satellite images were classified and composited over two days. To ensure accuracy, only pixels that showed a frequency of observed water bodies over two consecutive days of more than 0.5 were considered. Combining the images into a multi-day composite is necessary because it maximizes the elimination of misclassifications due to cloud shadows. Additionally, we used height above the nearest drainage (HAND) greater than 70 m as a mask to remove most of the error pixels caused by topographic shadows. The HAND metric provides a topography-based measure of local drainage potential that can mask water detected in areas that are physically unlikely to be flooded⁵¹.

The remaining water body pixels that lay outside the permanent water bodies defined by the global surface water dataset⁴⁹ were considered flooded. We calculated water bodies within the same flood inundation area for the same period each year within the closest six-year window around each flood event using the same algorithm. Pixels with a water body frequency less than 0.5 were defined as LFF areas, and pixels with a water body frequency greater than or equal to 0.5 were defined as HFF areas. We calculated the mean number of inundations across flood pixels for each flooding event within the window (Supplementary Fig. 7). We used the smallest integer greater than the mean number of inundations across all flood events (3; frequency = 0.5) as the threshold to classify LFF and HFF (Supplementary Fig. 8). Flood duration was defined as the difference between the latest and earliest dates in each pixel identified as a water body for a flood event. The processing was completed on Google Earth Engine:

$$\frac{\rho_{\text{nir}} + a}{\rho_{\text{red}} + b} < c \text{ and } \rho_{\text{red}} < d \text{ and } \rho_{\text{swir}} < e \quad (1)$$

where ρ_{nir} and ρ_{red} are the near-infrared and red bands from MOD/MYD09GQ061 at 250 m resolution, ρ_{swir} is the SWIR2 band from MOD/MYD09GA061 that is resampled to 250 m resolution, $a = 13.5$, $b = 1,081.1$, $c = 0.7$, $d = 2,027$, and $e = 675.7$. The values of a – e were determined empirically by DFO^{25,50}.

We provided two quality assessment reference layers for all global flood events and used the quality assessment bands of MOD09GA/MYD09GA to remove clouds from daily reflectance images. The proportion of clear observations during each flood event based on the quality assurance information is calculated to measure the uncertainty of the flood extraction results (Supplementary Fig. S8). The higher the quality assessment value, the potentially lower the uncertainty in mapping the flood inundation extent.

Accuracy evaluation and optimization of the flood database

We used the existing third-party flood validation points to assess accuracy of our generated global flood database²⁵. The 33,141 publicly available validation points for 123 flood events were obtained by manual visual interpretation using high-resolution (30 m) Landsat images (Supplementary Fig. 3). The validation points are distributed across latitudinal zones in multiple biomes and diverse landscapes²⁵. Accuracy metrics include omission error, commission error and accuracy. The calculations are as follows:

$$\text{accuracy} = \frac{\text{TP} + \text{TN}}{\text{TP} + \text{FN} + \text{FP} + \text{TN}} \quad (2)$$

$$\text{commission} = \frac{\text{FP}}{\text{TP} + \text{FP}} \quad (3)$$

$$\text{omission} = \frac{\text{FN}}{\text{TP} + \text{FN}} \quad (4)$$

where TP is true-positive count, TN is true-negative count, FN is false-negative count and FP is false-positive count.

The near-real-time flooding algorithm may overestimate the extent of flood inundation in high latitudes. Lower sun angles there generally lead to more cloud shadows identified as water bodies by mistake²⁶. To address this issue, we developed a new method to determine whether the flood inundation extent in high latitudes is overestimated. Specifically, we examined the accuracy of flood extent with different duration thresholds ranging from two to ten days with a one-day interval. Theoretically, if the flooding areas were overestimated, the validation accuracy would first increase and then decrease following the increased duration. If not, the accuracy would decrease gradually. We selected flood events across various latitudes for validating. Our

findings indicate that the validation accuracy at latitudes $>45^\circ$ does behave similarly to what we expect for the flooding areas being over-estimated. Furthermore, the global flooding areas extracted reach the highest accuracy with a duration threshold of four days and a latitude of 45° (Supplementary Figs. 4 and 5). We thus improved the original global flood database by retaining inundation extents with durations greater than four days at latitudes $>45^\circ$ among the 317 floods. As a result, the overall accuracy is 0.78, the commission error is 0.26 and the omission error is 0.21 (Supplementary Fig. 6).

Exploring patterns of global flooding of cropland

We used the global dynamic cropland data from Potapov et al.²⁰ to estimate the worldwide flood-affected cropland. The cropland was mapped every four years (2000–2003, 2004–2007, 2008–2011, 2012–2015 and 2016–2019) to diminish the influence of fallow cropland on the classification. We opted for this particular cropland dataset owing to its strict validation process and higher accuracy compared with other globally available cropland datasets⁵². Also, this dataset is consistent with FAO cropland statistics. The cropland area was resampled to 250 m to match the resolution of the flood database we generated. We overlaid the inundation area and duration layers for each flood event with the cropland layer to obtain the flood-affected cropland. For years without cropland data, we used data from the most recent year. The flooded cropland count was calculated by summing the pixels of flooded croplands for all flood events worldwide. With reference to a previous study⁵³, we defined the frequency of flooded cropland to represent the density of flooded cropland for all years by integrating the flooded cropland count and flooded cropland areas within $1^\circ \times 1^\circ$ grid cells in that year, which is expressed as:

$$\text{Frequency}_{\text{flooded cropland}} = \frac{n}{N} \sum_{i=1}^n M_i \quad (5)$$

where M_i is the flooded cropland count for the i th 250 m resolution pixel in all years (2000–2021) within one $1^\circ \times 1^\circ$ grid cell, n represents the associated number of flood-affected pixels in the same cell and N is the total number of 250 cropland pixels in this grid cell. We also calculated the maximum area and mean duration of global flooded cropland in a $1^\circ \times 1^\circ$ grid for different time periods.

Risk of cropland flooding due to changes in cropland

The absolute change method was used to analyse the relationship between the risk of flood-inundated cropland and cropland change. We intersected the recent maximum flood extent layer and the cropland change layer for two periods to analyse the increase (decrease) in flood-inundated cropland due to cropland expansion (contraction). We also calculated trends in total cropland area and cropland area affected by flooding using linear least squares regression (Supplementary Fig. 14).

Additionally, we analysed the changes in land use type in cropland flood exposure. We used the global flood maps generated and the global land use change data from 2000–2020 developed by Potapov et al.⁵⁴, and we conducted overlay and statistical analysis in the same years and at the same resolution (250 m). We used this land use change dataset because of its high classification accuracy, with user and producer accuracy rates exceeding 85% for all land cover and land use types except built-up land⁵⁴. The sources of cropland expansion are categorized into three types: trees (≥ 3 m height), wetlands and short vegetation (< 3 m height), and others⁵⁴.

Global crop yield statistics

We collected annual statistics on wheat and rice yield for 78 subnational regions (Supplementary Fig. 23). These data were obtained from official sources (Supplementary Table 12). The yield data cover the period 1998–2020. Statistics are missing for some years in some countries, but

we did not interpolate missing data using multi-year means because interpolated data could lead to erroneous evaluation results. We averaged sub-country yield statistics at the national level and confirmed that the yield trends are consistent with the FAO national-level yield. We did not use the FAO yield statistics data at the national level because floods usually affect crops only in local areas⁴. Higher-resolution crop yield data will therefore provide a more accurate assessment.

Assessing the impacts of flooding on crop yields

We chose administrative units as samples to analyse the mean percentage crop yield anomalies in the LFF and HFF areas⁴. First, we excluded samples with less than 7.5% flooded cropland in the total cropland for each flood event. The remaining samples, where the percentage of flooded cropland area (LFF or HFF) exceeds 70% of the total flooded crop area, were used to examine the crop yield anomalies (LFF or HFF samples).

The yield anomalies relative to long-term trend yields ($Y'_{t,c,f,s}$) were calculated as follows:

$$Y'_{t,c,f,s} = \frac{Y_{t,c,f,s} - \bar{Y}_{t,c,f,s}}{\bar{Y}_{t,c,f,s}} \times 100 \quad (6)$$

$$\bar{Y}_{t,c,f,s} = \frac{1}{5} \sum_{i=-2}^2 Y_{t+i,c,f,s} \quad (7)$$

where t, c, f and s are year, crop (wheat and rice), flood type (LFF and HFF) and sample unit, respectively. $Y_{t,c,f,s}$ is the recorded yield, and $\bar{Y}_{t,c,f,s}$ is the five-year central moving mean. The calculation of yield anomalies eliminates yield trends caused by non-climatic factors (that is, technical and other factors) to emphasize yield changes caused by short-term factors (mainly disaster-related factors)^{55,56}.

We used the synthetic analysis method to compare the mean values of yield anomalies during flood years with those during non-flood years. This allowed us to identify significant characteristics of yield anomalies during flood years:

$$Y'_{\text{Flood},c,f,s} = \frac{1}{n_{\text{Flood},c,f,s}} \sum_{t=y_{\text{start}}}^{y_{\text{end}}} Y'_{t,\text{Flood},c,f,s} \quad (8)$$

$$Y'_{\text{non-Flood},c,f,s} = \frac{1}{n_{\text{non-Flood},c,f,s}} \sum_{t=y_{\text{start}}}^{y_{\text{end}}} Y'_{t,\text{non-Flood},c,f,s} \quad (9)$$

where $Y'_{\text{Flood},c,f,s}$ and $Y'_{\text{non-Flood},c,f,s}$ are the mean percentage yield anomalies (%) in flood and non-flood years, respectively; $n_{\text{Flood},c,f,s}$ and $n_{\text{non-Flood},c,f,s}$ are the number of flood and non-flood years, respectively; $Y'_{t,\text{Flood},c,f,s}$ and $Y'_{t,\text{non-Flood},c,f,s}$ are the yield anomalies in year t with and without flood events, respectively; and y_{start} and y_{end} are the start year (2000) and end year (2019) of the study period, respectively.

Finally, the difference between the mean percentage yield anomalies in flood and non-flood years ($\Delta Y'_{\text{Flood},c,f,s}$) was calculated. Negative values indicate the mean negative effect of flooding on yield, and positive values indicate the mean positive effect. The processing was completed in MATLAB (version 2022a) and Microsoft Excel (version 2021):

$$\Delta Y'_{\text{Flood},c,f,s} = Y'_{\text{Flood},c,f,s} - Y'_{\text{non-Flood},c,f,s} \quad (10)$$

Testing the significance of flood impacts on crop yields

We tested the significance of $\Delta Y'_{\text{Flood},c,f,s}$ for each sample using the bootstrap method⁵⁶. First, we pooled all $Y'_{t,\text{Flood},c,f,s}$ and $Y'_{t,\text{non-Flood},c,f,s}$ within the sample. Second, sampling ($n \sim U(1, n_{\text{Flood}/\text{non-Flood},c,f,s})$) was performed separately in the flood and non-flood years of the sample. On the basis of equations (8) and (9), $Y'_{\text{Flood},c,f,s}$ and $Y'_{\text{non-Flood},c,f,s}$ were

obtained. Third, equation (10) was used to obtain $\Delta Y'_{\text{Flood},c,f,s}$. Fourth, we iterated 10,000 times for sample $\Delta Y'_{\text{Flood},c,f,s}$ and counted the number of rejections of the original hypothesis. The ratio of the number of rejections of the original hypothesis to the total number of samples is the bootstrap probability or *P* value. On the basis of previous studies, we set the significance level at 10%⁵⁶.

Significance test on differences among groups

We used the Wilcoxon test to assess the statistical significance of anomalous differences in mean crop yield (%) in LFF and HFF areas. The statistical tests were two-sided, and no adjustments were made for multiple comparisons. We did not use parametric statistical tests assuming normal distribution because we rejected the null hypothesis of normality for all groups at the 5% significance level using the Anderson–Darling normality test. The Wilcoxon test for significance of differences between group distributions (not assuming normality) includes differences in medians and variances. The application of Levene's test to the square of the data shows equal variance between groups for LFF and HFF for wheat and rice (significance at 5%). In the case of significant differences and equal variances between groups, we can conclude that the significant differences are caused by the median.

Crop phenology at the time of flooding

We used a phenology product (MCD12Q2) based on remote sensing to identify crop phenology at the beginning and end of each flood event for all cropland pixels inundated. The 500 m resolution MCD12Q2 data for each year are based on the EVI2 time series, which identify six key phenological transition dates for each crop growth cycle (Supplementary Fig. 31)⁵⁷. We defined the period between 'MidGreenup' and 'MidGreendown' as the crop's GS. We used the median phenology of the six years closest to the year of the flood event as the normal phenology of the crop unaffected by the flood. We then calculated the normal phenology of the flooded crop at the beginning and end of the flood. We did not use the phenology of the flood years because floods can affect crop growth, and in cases where crop growth is severely damaged, MCD12Q2 will not be able to identify the phenological stages of vegetation. To check the robustness of the conclusions, we also used the Global Gridded Crop Model Intercomparison Phase III crop calendar product, which is a comprehensive crop calendar that integrates multiple data sources³² and provides multi-year mean planting and maturity dates for various crops in each $0.5^\circ \times 0.5^\circ$ grid cell.

Crop growth anomalies after flooding

We analysed the impacts of floods on vegetation growth in both the short and long term. We used 250 m MOD09Q1 spectral reflectance data from 2000–2022. We used the quality assurance band to remove image clouds and shadow pixels to obtain clear, cloud-free images. We calculated the EVI2 time series and used a moving average filter to fill in missing values (EVI2 was used because it is not easily saturated with the dense vegetation canopy⁵⁸):

$$\text{EVI2} = 2.5 \times \frac{\rho_{\text{nir}} - \rho_{\text{red}}}{\rho_{\text{nir}} + 2.4 \times \rho_{\text{red}} + 1} \quad (11)$$

where ρ_{nir} and ρ_{red} are the near-infrared band and red band reflectance, respectively.

We extracted the flooding pixels where the growing crop was in its vegetative stage at the beginning of a flood event. The vegetative stage is defined as the pre-growth period before the 'peak'⁵⁷. We analysed both short-term and long-term growth anomalies of these pixels after the flood:

$$\text{EVI2}_{\text{anomalies},y} = \Delta \text{EVI}_y, \text{ if } \Delta \text{EVI}_y < 0 \quad (12)$$

$$\Delta \text{EVI}_y = \text{EVI}_{\text{max},y} - (\text{mEVI}_y - \text{s.d.EVI}_y) \quad (13)$$

$$\text{EVI}_{\text{max},y} = \max(\text{EVI}_{y,m}) \quad (14)$$

$$\text{mEVI}_y = \text{median}(\text{EVI}_{\text{max},y-\text{win}}) \quad (15)$$

$$\text{s.d.EVI}_y = \text{s.d.}(\text{EVI}_{\text{max},y-\text{win}}) \quad (16)$$

where crop growth anomalies ($\text{EVI2}_{\text{anomalies}}$) are defined as EVI2 's maximum ($\text{EVI}_{\text{max},y}$) for m months after a flood that is significantly lower than its normal range's minimum. This minimum (ΔEVI_y) is defined as the median of EVI2 's maximum values (mEVI_y) for six years surrounding a flood year (y) during that same period minus three times its standard deviation (s.d.EVI_y). The win values are $-3, -2, -1, 1, 2$ and 3 . For calculations of short-term growth anomalies, $m = 1$; to calculate long-term growth anomalies, we set different m values depending on cropping intensity to ensure that the calculated growth variation is in sync with the crop cycle at the time of the flood (the m values are 11, 5 and 3 for single, double and triple seasons, respectively). Cropping intensity data were obtained from MCD12Q2 (ref. 57). We calculated crop growth anomalies for all flood events.

PA/SMA in floods

We calculated PA/SMA for each flood event using several data products. The precipitation data include satellite precipitation products (CHIRPS and IMERG) as well as reanalysis data products (ERA5-Land). CHIRPS has a long record period, high spatial resolution (0.05°), low spatial bias and low time delay, and it has been widely used for extreme precipitation analysis in South Asia due to its proven record of high accuracy in precipitation products⁵⁹. IMERG is derived using the IMERG algorithm in combination with observations from several passive microwave satellites in the GPM constellation, which can accurately capture the spatial and temporal variability of precipitation in the tropics⁶⁰. ERA5-Land combines model data with observations from around the world to create a globally complete and consistent dataset⁶¹. We used the soil moisture in the soil layer from ERA5-Land at various depths. All satellite and reanalysis products are accumulated on a daily scale.

We extracted cumulative precipitation and soil moisture data for the period from the beginning to the end of the flood, including three years before and after the hazard for that same period. PA/SMA were defined by normalizing flood year data to the average of the preceding and succeeding three years to remove the regional climatic context. We counted PA/SMA for each unit of analysis in each flood event.

Sensitivity and uncertainty analysis

We carried out sensitivity analyses focused on several key aspects: the sensitivity of flood-affected cropland areas to missing data on flood events (Supplementary Method 1), the influence of sample size on our results (Supplementary Method 2) and the sensitivity to the thresholds in classifying LFF and HFF (Supplementary Method 3). Moreover, we quantified the uncertainties propagated from flood mapping to crop yield losses (Supplementary Method 4). For methodological details, refer to the Supplementary Methods.

Reporting summary

Further information on research design is available in the Nature Portfolio Reporting Summary linked to this article.

Data availability

The global flood events database from the DFO is accessible at <https://floodobservatory.colorado.edu/temp/>. The HydroSHEDS Basins Level 6 watersheds database is accessible at https://developers.google.com/earth-engine/datasets/catalog/WWF_HydroSHEDS_v1_Basins_hybas_6#description. The HAND data are accessible at <https://gee-community-catalog.org/projects/hand/>. MOD09GQ is accessible at <https://developers.google.com/earth-engine/datasets/>

catalog/MODIS_061_MOD09GQ. MYD09GQ is accessible at https://developers.google.com/earth-engine/datasets/catalog/MODIS_061_MYD09GQ. MOD09GA is accessible at https://developers.google.com/earth-engine/datasets/catalog/MODIS_061_MOD09GA. MYD09GA is accessible at https://developers.google.com/earth-engine/datasets/catalog/MODIS_061_MYD09GA. MCD12Q2 is accessible at https://developers.google.com/earth-engine/datasets/catalog/MODIS_061_MCD12Q2. MOD09Q1 is accessible at https://developers.google.com/earth-engine/datasets/catalog/MODIS_061_MOD09Q1. The global surface water dataset is accessible at https://developers.google.com/earth-engine/datasets/catalog/JRC_GSW1_4_YearlyHistory#description. The cropland datasets are accessible at <https://glad.umd.edu/dataset/croplands>. The flood verification points are accessible at https://github.com/cloudtostreet/MODIS_GlobalFloodDatabase. The crop calendar product (GGCMI Phase III) is accessible via Zenodo at <https://doi.org/10.5281/zenodo.5062513> (ref. 62). CHIRPS is accessible at https://developers.google.com/earth-engine/datasets/catalog/UCSB-CHG_CHIRPS_DAILY. IMERG is accessible at https://developers.google.com/earth-engine/datasets/catalog/NASA_GPM_L3_IMERG_V06. ERA5-Land is accessible at https://developers.google.com/earth-engine/datasets/catalog/ECMWF_ERA5_LAND_DAILY_AGGR. The crop area datasets are accessible at <https://mapspam.info/>. The global land cover and land use change datasets are accessible at <https://glad.umd.edu/dataset/GLCLUC2020>. Spatial data for all countries and their subdivisions are available at <https://gadm.org/>. The crop yield data are available in the Supplementary Information (Supplementary Table 12).

Code availability

The key code for mapping the inundation extent and duration of global flood events is available via Zenodo at <https://doi.org/10.5281/zenodo.11181120> (ref. 63).

References

- Qamer, F. M. et al. A framework for multi-sensor satellite data to evaluate crop production losses: the case study of 2022 Pakistan floods. *Sci. Rep.* **13**, 4240 (2023).
- Dryden, R., Anand, M., Lehner, B. & Fluet-Chouinard, E. Do we prioritize floodplains for development and farming? Mapping global dependence and exposure to inundation. *Glob. Environ. Change* **71**, 102370 (2021).
- Kim, W., Iizumi, T. & Nishimori, M. Global patterns of crop production losses associated with droughts from 1983 to 2009. *J. Appl. Meteorol. Climatol.* **58**, 1233–1244 (2019).
- Lesk, C., Rowhani, P. & Ramankutty, N. Influence of extreme weather disasters on global crop production. *Nature* **529**, 84–87 (2016).
- Schewe, J. et al. State-of-the-art global models underestimate impacts from climate extremes. *Nat. Commun.* **10**, 1005 (2019).
- Liu, K. et al. Silver lining to a climate crisis in multiple prospects for alleviating crop waterlogging under future climates. *Nat. Commun.* **14**, 765 (2023).
- Li, Y., Guan, K., Schnitkey, G. D., DeLucia, E. & Peng, B. Excessive rainfall leads to maize yield loss of a comparable magnitude to extreme drought in the United States. *Glob. Change Biol.* **25**, 2325–2337 (2019).
- Hirabayashi, Y., Tanoue, M., Sasaki, O., Zhou, X. & Yamazaki, D. Global exposure to flooding from the new CMIP6 climate model projections. *Sci. Rep.* **11**, 3740 (2021).
- Rodell, M. & Li, B. Changing intensity of hydroclimatic extreme events revealed by GRACE and GRACE-FO. *Nat. Water* **1**, 241–248 (2023).
- Zhang, S. et al. Reconciling disagreement on global river flood changes in a warming climate. *Nat. Clim. Change* **12**, 1160–1167 (2022).
- Chen, H., Liang, Q., Liang, Z., Liu, Y. & Xie, S. Remote-sensing disturbance detection index to identify spatio-temporal varying flood impact on crop production. *Agric. For. Meteorol.* **269–270**, 180–191 (2019).
- Li, S., Tompkins, A. M., Lin, E. & Ju, H. Simulating the impact of flooding on wheat yield—case study in East China. *Agric. For. Meteorol.* **216**, 221–231 (2016).
- Shirzaei, M. et al. Persistent impact of spring floods on crop loss in U.S. Midwest. *Weather Clim. Extrem.* **34**, 100392 (2021).
- Fu, J. et al. Extreme rainfall reduces one-twelfth of China's rice yield over the last two decades. *Nat. Food* <https://doi.org/10.1038/s43016-023-00753-6> (2023).
- Kim, W., Iizumi, T., Hosokawa, N., Tanoue, M. & Hirabayashi, Y. Flood impacts on global crop production: advances and limitations. *Environ. Res. Lett.* **18**, 054007 (2023).
- Venkatappa, M., Sasaki, N., Han, P. & Abe, I. Impacts of droughts and floods on croplands and crop production in Southeast Asia—an application of Google Earth Engine. *Sci. Total Environ.* **795**, 148829 (2021).
- Ray, D. K. et al. Climate change has likely already affected global food production. *PLoS ONE* **14**, e0217148 (2019).
- Martinis, S., Groth, S., Wieland, M., Knopp, L. & Röttich, M. Towards a global seasonal and permanent reference water product from Sentinel-1/2 data for improved flood mapping. *Remote Sens. Environ.* **278**, 113077 (2022).
- Pekel, J.-F., Cottam, A., Gorelick, N. & Belward, A. S. High-resolution mapping of global surface water and its long-term changes. *Nature* **540**, 418–422 (2016).
- Potapov, P. et al. Global maps of cropland extent and change show accelerated cropland expansion in the twenty-first century. *Nat. Food* **3**, 19–28 (2022).
- Banerjee, L. Effects of flood on agricultural productivity in Bangladesh. *Oxf. Dev. Stud.* **38**, 339–356 (2010).
- Reed, C. et al. The impact of flooding on food security across Africa. *Proc. Natl Acad. Sci. USA* **119**, e2119399119 (2022).
- Yin, J. et al. Flash floods: why are more of them devastating the world's driest regions? *Nature* **615**, 212–215 (2023).
- Policelli, F. et al. The NASA Global Flood Mapping System. in *Remote Sensing of Hydrological Extremes* (ed. Lakshmi, V.) 47–63 (Springer, 2017).
- Tellman, B. et al. Satellite imaging reveals increased proportion of population exposed to floods. *Nature* **596**, 80–86 (2021).
- Nigro, J., Slayback, D., Policelli, F. & Brakenridge, G. R. NASA/ DFO MODIS near real-time (NRT) global flood mapping product evaluation of flood and permanent water detection. Technical Report 1–27 (NASA Goddard Space Flight Center, 2014).
- Hansen, M. C. et al. Global land use extent and dispersion within natural land cover using Landsat data. *Environ. Res. Lett.* **17**, 034050 (2022).
- Song, X.-P. et al. Global land change from 1982 to 2016. *Nature* **560**, 639–643 (2018).
- Zhang, S. & Wang, B. Global summer monsoon rainy seasons. *Int. J. Climatol.* **28**, 1563–1578 (2008).
- Balke, T. & Nilsson, C. Increasing synchrony of annual river-flood peaks and growing season in Europe. *Geophys. Res. Lett.* **46**, 10446–10453 (2019).
- Ficchi, A. & Stephens, L. Climate variability alters flood timing across Africa. *Geophys. Res. Lett.* **46**, 8809–8819 (2019).
- Jägermeyr, J. et al. Climate impacts on global agriculture emerge earlier in new generation of climate and crop models. *Nat. Food* **2**, 873–885 (2021).
- Cea, L. & Fraga, I. Incorporating antecedent moisture conditions and intraevent variability of rainfall on flood frequency analysis in poorly gauged basins. *Water Resour. Res.* **54**, 8774–8791 (2018).

34. Wasko, C., Nathan, R. & Peel, M. C. Changes in antecedent soil moisture modulate flood seasonality in a changing climate. *Water Resour. Res.* **56**, e2019WR026300 (2020).
35. Tramblay, Y., Villarini, G., El Khalki, E. M., Gründemann, G. & Hughes, D. Evaluation of the drivers responsible for flooding in Africa. *Water Resour. Res.* **57**, e2021WR029595 (2021).
36. Bofana, J. et al. How long did crops survive from floods caused by Cyclone Idai in Mozambique detected with multi-satellite data. *Remote Sens. Environ.* **269**, 112808 (2022).
37. Shrestha, B. B., Kawasaki, A. & Zin, W. W. Development of flood damage functions for agricultural crops and their applicability in regions of Asia. *J. Hydrol. Reg. Stud.* **36**, 100872 (2021).
38. Bolton, D. K. & Friedl, M. A. Forecasting crop yield using remotely sensed vegetation indices and crop phenology metrics. *Agric. For. Meteorol.* **173**, 74–84 (2013).
39. Tangdamrongsub, N., Forgotson, C., Gangodagamage, C. & Forgotson, J. The analysis of using satellite soil moisture observations for flood detection, evaluating over the Thailand's Great Flood of 2011. *Nat. Hazards* **108**, 2879–2904 (2021).
40. Pyka, L., Al-Maruf, A., Shamsuzzoha, M., Jenkins, J. & Braun, B. Floating gardening in coastal Bangladesh: evidence of sustainable farming for food security under climate change. *J. Agric. Food Environ.* **1**, 161–168 (2020).
41. Varela, R. P., Apdohan, A. G. & Balanay, R. M. Climate resilient agriculture and enhancing food production: field experience from Agusan del Norte, Caraga Region, Philippines. *Front. Sustain. Food Syst.* **6**, 974789 (2022).
42. Gommers, R., Wu, B., Li, Z. & Zeng, H. Design and characterization of spatial units for monitoring global impacts of environmental factors on major crops and food security. *Food Energy Secur.* **5**, 40–55 (2016).
43. Spence, A., Poortinga, W., Butler, C. & Pidgeon, N. F. Perceptions of climate change and willingness to save energy related to flood experience. *Nat. Clim. Change* **1**, 46–49 (2011).
44. Hirst, S. M. & Ibrahim, A. M. Effects of flood protection on soil fertility in a Riverine floodplain area in Bangladesh. *Commun. Soil Sci. Plant Anal.* **27**, 119–156 (1996).
45. Kaur, G. et al. Impacts and management strategies for crop production in waterlogged or flooded soils: a review. *Agron. J.* **112**, 1475–1501 (2020).
46. Sharma, R. K. et al. Impact of recent climate change on corn, rice, and wheat in southeastern USA. *Sci. Rep.* **12**, 16928 (2022).
47. Najibi, N. & Devineni, N. Recent trends in the frequency and duration of global floods. *Earth Syst. Dyn.* **9**, 757–783 (2018).
48. He, X., Pan, M., Wei, Z., Wood, E. F. & Sheffield, J. A global drought and flood catalogue from 1950 to 2016. *Bull. Am. Meteorol. Soc.* **101**, E508–E535 (2020).
49. Lehner, B. & Grill, G. Global river hydrography and network routing: baseline data and new approaches to study the world's large river systems. *Hydrol. Process.* **27**, 2171–2186 (2013).
50. Marsalek, J., Stancalie, G. & Balint, G. *Transboundary Floods: Reducing Risks through Flood Management* Vol. 72 (Springer Science & Business Media, 2006).
51. Nobre, A. D. et al. HAND contour: a new proxy predictor of inundation extent. *Hydrol. Process.* **30**, 320–333 (2016).
52. Meng, Z. et al. Post-2020 biodiversity framework challenged by cropland expansion in protected areas. *Nat. Sustain.* <https://doi.org/10.1038/s41893-023-01093-w> (2023).
53. Dai, Y. Coastal phytoplankton blooms expand and intensify in the 21st century. *Nature* **615**, 280–284 (2023).
54. Potapov, P. et al. The global 2000–2020 land cover and land use change dataset derived from the Landsat archive: first results. *Front. Remote Sens.* **3**, 856903 (2022).
55. Cao, J. et al. Forecasting global crop yields based on El Nino Southern Oscillation early signals. *Agric. Syst.* **205**, 103564 (2023).
56. Iizumi, T. et al. Impacts of El Niño Southern Oscillation on the global yields of major crops. *Nat. Commun.* **5**, 3712 (2014).
57. Gray, J., Sulla-Menashe, D. & Friedl, M. A. *User Guide to Collection 6 MODIS Land Cover Dynamics (MCD12Q2) Product* (NASA EOSDIS LP DAAC, 2019).
58. Jiang, Z., Huete, A., Didan, K. & Miura, T. Development of a two-band enhanced vegetation index without a blue band. *Remote Sens. Environ.* **112**, 3833–3845 (2008).
59. Funk, C. et al. The climate hazards infrared precipitation with stations—a new environmental record for monitoring extremes. *Sci. Data* **2**, 150066 (2015).
60. Pradhan, R. K. et al. Review of GPM IMERG performance: a global perspective. *Remote Sens. Environ.* **268**, 112754 (2022).
61. Muñoz-Sabater, J. et al. ERA5-Land: a state-of-the-art global reanalysis dataset for land applications. *Earth Syst. Sci. Data* **13**, 4349–4383 (2021).
62. Jägermeyr, J., Müller, C., Minoli, S., Ray, D. & Siebert, S. GGCM Phase 3 crop calendar. *Zenodo* <https://doi.org/10.5281/zenodo.5062513> (2021).
63. Han, J., & Zhang, Z. The code for mapping the inundation extent and duration of flood events. *Zenodo* <https://doi.org/10.5281/zenodo.11181120> (2024).

Acknowledgements

We acknowledge financial support from the National Natural Science Foundation of China (grant nos 42061144003 (Z.Z.) and 42301187 (J.X.)) and the CAS-CSRIO cooperation project (grant no.177GJHZ2022052MI (F.T.)).

Author contributions

Z.Z., F.T. and J.H. conceptualized the project. J.H., Z.Z., J.X. and J.C. designed the methodology. J.H., Y.C., J.C., Y.L. and F.C. undertook the formal analyses. J.H., J.C., Z.Z., Y.C. and H.Z. performed the investigations. Z.Z. and F.T. supervised the work. J.H., J.X. and J.C. validated the results. J.H., H.W., Q.M. and J.S. visualized the data. J.H., Z.Z. and F.T. wrote the first draft. J.J., Z.Z., F.T. and J.X. contributed to the review and editing of the paper.

Competing interests

The authors declare no competing interests.

Additional information

Supplementary information The online version contains supplementary material available at <https://doi.org/10.1038/s41893-024-01375-x>.

Correspondence and requests for materials should be addressed to Zhao Zhang or Fulu Tao.

Peer review information *Nature Sustainability* thanks Sawaid Abbas, Manoochehr Shirzaei and Feng Zhou for their contribution to the peer review of this work.

Reprints and permissions information is available at www.nature.com/reprints.

Publisher's note Springer Nature remains neutral with regard to jurisdictional claims in published maps and institutional affiliations.

Springer Nature or its licensor (e.g. a society or other partner) holds exclusive rights to this article under a publishing agreement with the author(s) or other rightsholder(s); author self-archiving of the accepted manuscript version of this article is solely governed by the terms of such publishing agreement and applicable law.

© The Author(s), under exclusive licence to Springer Nature Limited 2024

Reporting Summary

Nature Portfolio wishes to improve the reproducibility of the work that we publish. This form provides structure for consistency and transparency in reporting. For further information on Nature Portfolio policies, see our [Editorial Policies](#) and the [Editorial Policy Checklist](#).

Statistics

For all statistical analyses, confirm that the following items are present in the figure legend, table legend, main text, or Methods section.

n/a Confirmed

- | | | |
|-------------------------------------|-------------------------------------|------------------------------------------------------------------------------------------------------------------------------------------------------------------------------------------------------------------------------------------------------------|
| <input type="checkbox"/> | <input checked="" type="checkbox"/> | The exact sample size (n) for each experimental group/condition, given as a discrete number and unit of measurement |
| <input checked="" type="checkbox"/> | <input type="checkbox"/> | A statement on whether measurements were taken from distinct samples or whether the same sample was measured repeatedly |
| <input type="checkbox"/> | <input checked="" type="checkbox"/> | The statistical test(s) used AND whether they are one- or two-sided
<i>Only common tests should be described solely by name; describe more complex techniques in the Methods section.</i> |
| <input type="checkbox"/> | <input checked="" type="checkbox"/> | A description of all covariates tested |
| <input type="checkbox"/> | <input checked="" type="checkbox"/> | A description of any assumptions or corrections, such as tests of normality and adjustment for multiple comparisons |
| <input type="checkbox"/> | <input checked="" type="checkbox"/> | A full description of the statistical parameters including central tendency (e.g. means) or other basic estimates (e.g. regression coefficient) AND variation (e.g. standard deviation) or associated estimates of uncertainty (e.g. confidence intervals) |
| <input type="checkbox"/> | <input checked="" type="checkbox"/> | For null hypothesis testing, the test statistic (e.g. F , t , r) with confidence intervals, effect sizes, degrees of freedom and P value noted
<i>Give P values as exact values whenever suitable.</i> |
| <input checked="" type="checkbox"/> | <input type="checkbox"/> | For Bayesian analysis, information on the choice of priors and Markov chain Monte Carlo settings |
| <input type="checkbox"/> | <input checked="" type="checkbox"/> | For hierarchical and complex designs, identification of the appropriate level for tests and full reporting of outcomes |
| <input checked="" type="checkbox"/> | <input type="checkbox"/> | Estimates of effect sizes (e.g. Cohen's d , Pearson's r), indicating how they were calculated |

Our web collection on [statistics for biologists](#) contains articles on many of the points above.

Software and code

Policy information about [availability of computer code](#)

Data collection No software was used for data collection

Data analysis All data processing and analysis were conducted in Google Earth Engine, MATLAB (version 2022a), and Microsoft Excel (version 2021).

For manuscripts utilizing custom algorithms or software that are central to the research but not yet described in published literature, software must be made available to editors and reviewers. We strongly encourage code deposition in a community repository (e.g. GitHub). See the Nature Portfolio [guidelines for submitting code & software](#) for further information.

Data

Policy information about [availability of data](#)

All manuscripts must include a [data availability statement](#). This statement should provide the following information, where applicable:

- Accession codes, unique identifiers, or web links for publicly available datasets
- A description of any restrictions on data availability
- For clinical datasets or third party data, please ensure that the statement adheres to our [policy](#)

Data Availability

Global flood events database from the Dartmouth Flood Observatory (DFO) is accessible at <https://floodobservatory.colorado.edu/temp/>.
HydroSHEDS Basins Level 6 watersheds database is accessible at https://developers.google.com/earth-engine/datasets/catalog/WWF_HydroSHEDS_v1_Basins_hybas_6#description.

Height above the nearest drainage (HAND) data are accessible at <https://gee-community-catalog.org/projects/hand/>.
 MOD09GQ is accessible at https://developers.google.com/earth-engine/datasets/catalog/MODIS_061_MOD09GQ.
 MYD09GQ is accessible at https://developers.google.com/earth-engine/datasets/catalog/MODIS_061_MYD09GQ.
 MOD09GA is accessible at https://developers.google.com/earth-engine/datasets/catalog/MODIS_061_MOD09GA.
 MYD09GA is accessible at https://developers.google.com/earth-engine/datasets/catalog/MODIS_061_MYD09GA.
 MCD12Q2 is accessible at https://developers.google.com/earth-engine/datasets/catalog/MODIS_061_MCD12Q2.
 MOD09Q1 is accessible at https://developers.google.com/earth-engine/datasets/catalog/MODIS_061_MOD09Q1.
 Global surface water dataset is accessible at https://developers.google.com/earth-engine/datasets/catalog/JRC_GSW1_4_YearlyHistory#description.
 Cropland datasets are accessible at <https://glad.umd.edu/dataset/croplands>.
 Flood verification points is accessible at https://github.com/cloudtostreet/MODIS_GlobalFloodDatabase.
 Crop calendar product (GGCMI Phase III) is accessible at <https://zenodo.org/record/5062513>.
 CHIRPS is accessible at https://developers.google.com/earth-engine/datasets/catalog/UCSB-CHG_CHIRPS_DAILY.
 IMERG is accessible at https://developers.google.com/earth-engine/datasets/catalog/NASA_GPM_L3_IMERG_V06.
 ERA5-Land is accessible at https://developers.google.com/earth-engine/datasets/catalog/ECMWF_ERA5_LAND_DAILY_AGGR.
 Crop area datasets are accessible at <https://mapspam.info/>.
 Global land cover and land use change datasets are accessible at <https://glad.umd.edu/dataset/GLCLUC2020>.
 Spatial data for all countries and their subdivisions are available at <https://gadm.org/>.

Human research participants

Policy information about [studies involving human research participants and Sex and Gender in Research](#).

Reporting on sex and gender

n/a

Population characteristics

n/a

Recruitment

n/a

Ethics oversight

n/a

Note that full information on the approval of the study protocol must also be provided in the manuscript.

Field-specific reporting

Please select the one below that is the best fit for your research. If you are not sure, read the appropriate sections before making your selection.

☐ Life sciences

☐ Behavioural & social sciences

☒ Ecological, evolutionary & environmental sciences

For a reference copy of the document with all sections, see [nature.com/documents/nr-reporting-summary-flat.pdf](https://www.nature.com/documents/nr-reporting-summary-flat.pdf)

Ecological, evolutionary & environmental sciences study design

All studies must disclose on these points even when the disclosure is negative.

Study description

We used satellite imagery to map the global spatial distributions of low-frequency flood (LFF) and high-frequency flood (HFF) events, assessing their impacts on cropland and crop yields. We also analyzed the potential influencing factors for the differences in crop yield losses between LFF and HFF areas.

Research sample

Our analysis covered 3,427 flood events from 2000 to 2021 with a high resolution of 250 meters. We collected annual statistics on wheat and rice yield for 78 sub-countries. We obtained the sample for analyzing the impact of floods on crop yields based on global flood maps and crop yield statistics.

Sampling strategy

All available samples meeting the calculation criteria.

Data collection

All the data used for this study were downloaded from international organizations, public databases, and peer-reviewed papers.

Timing and spatial scale

n/a

Data exclusions

None.

Reproducibility

We have provided data source information to ensure reproducibility.

Randomization

n/a

Blinding

n/a

Did the study involve field work? ☐ Yes ☒ No

Reporting for specific materials, systems and methods

We require information from authors about some types of materials, experimental systems and methods used in many studies. Here, indicate whether each material, system or method listed is relevant to your study. If you are not sure if a list item applies to your research, read the appropriate section before selecting a response.

Materials & experimental systems

n/a	Involved in the study
<input checked="" type="checkbox"/>	<input type="checkbox"/> Antibodies
<input checked="" type="checkbox"/>	<input type="checkbox"/> Eukaryotic cell lines
<input checked="" type="checkbox"/>	<input type="checkbox"/> Palaeontology and archaeology
<input checked="" type="checkbox"/>	<input type="checkbox"/> Animals and other organisms
<input checked="" type="checkbox"/>	<input type="checkbox"/> Clinical data
<input checked="" type="checkbox"/>	<input type="checkbox"/> Dual use research of concern

Methods

n/a	Involved in the study
<input checked="" type="checkbox"/>	<input type="checkbox"/> ChIP-seq
<input checked="" type="checkbox"/>	<input type="checkbox"/> Flow cytometry
<input checked="" type="checkbox"/>	<input type="checkbox"/> MRI-based neuroimaging